

Meandering Microstrip Leaky-Wave Antenna with Dual-band Linear–Circular Polarization and Suppressed Open Stopband

Pratik Vadher, Giulia Sacco, and Denys Nikolayev

Abstract—This paper proposes a dual-band frequency scanning meandering microstrip leaky-wave antenna with linear polarization in the Ku-band and circular polarization in the K-band. This is achieved by making use of two spatial harmonics for radiation. The unit cell of the periodic microstrip antenna contains three meanders with mitered corners. To ensure circular polarization, a theoretical formulation is developed taking into account the delay caused by microstrip length intervals. It defines the unit cell geometry by determining the length of the meanders to ensure that axial ratio remains below 3 dB throughout the operational band. Moreover, the meanders are used to provide better control over scanning rate (the ratio of change of angle of maximum radiation with frequency) and reduce spurious radiation of harmonics by ensuring single harmonic operation within the operational band. To guarantee continuous scanning through broadside direction, open stopband is suppressed using mitered angles. The antenna is designed on a 0.254-mm substrate making it suitable for conformal applications. The fabricated antenna shows a backward to forward beam steering range of 72° (−42° to 30°) in the K-band (19.4–27.5 GHz) with circular polarization and of 75° (−15° to 60°) in the Ku-band (11–15.5 GHz) with linear polarization.

Index Terms—leaky wave antenna (LWA), Ku-band, K-band, higher spatial order, scanning rate, meandering microstrip antenna

I. INTRODUCTION

Periodic leaky wave antennas (LWAs) are a class of travelling-wave antennas that radiate energy at the discontinuities of the guiding medium [1]. Changes in frequency causes dispersion within the guiding medium, resulting in varying excitation phases at the discontinuities. This, in turn, alters the main beam pointing direction in the radiation pattern of the antenna with respect to frequency. One-dimensional periodic LWAs (1D LWAs) typically radiate a fan-beam in the E-plane. The direction of maximum radiation changes in the H-plane with the change in frequency [2].

Many 1D periodic LWAs have been proposed using different guiding media. LWAs proposed in [3–7] use substrate integrated waveguide (SIW) or half-mode SIW to support the

Manuscript received April 25, 2023.

This study was supported in part by the French Agence Nationale de la Recherche (ANR) through the Project MedWave under Grant ANR-21-CE19-0045; in part by the European Union’s Horizon 2020 research and innovation program under the Marie Skłodowska-Curie N°899546 grant through the REACH-IT project; and in part by the European Union’s Horizon Europe research and innovation program through the Marie Skłodowska-Curie IN-SIGHT project N°101063966. (Corresponding author: Denys Nikolayev, denys.nikolayev@deniq.com)

P. Vadher, G. Sacco, and D. Nikolayev are with the Univ Rennes, CNRS, IETR – UMR 6164, FR-35000 Rennes, France.

travelling wave and usually employ a TE_{n0} or in certain cases TM_{11} mode [8] for radiation. However, to reduce fabrication complexity, lower manufacturing costs, and to enable the creation of compact antennas, microstrip-based guiding media LWAs are an appealing solution [9–13]. Meandering microstrip LWAs radiate due to the discontinuities created at the edges which results in a net magnetic current responsible for radiation [13], [14].

Since LWAs are periodic structures, infinite spatial harmonics exist in the guiding media [2], [15]. Many SIW based LWAs that use higher order Floquet modes for radiation have been proposed recently [16], [17]. Although the previous works report scanning due to higher spatial harmonics, the scanning is due to two or three spatial harmonics at the same time, which leads to more than one beam radiated by the antenna. However, it is desirable to have a single beam scanning operation over a high scanning range. This is possible when only a single spatial harmonic is responsible for radiation. Hence, better separation of different spatial harmonics is necessary.

To be suitable for on-body conformal applications [18–21], the antenna must be flexible and bendable [22]. For such a purpose, antennas based on microstrip technology are an excellent candidate. Additionally, the mechanical properties such as tensile modulus of the dielectric substrate also play an important factor. Hence, the Rogers 3003 substrate ($\epsilon_r = 3.0$) is preferred in this work due to its low tensile modulus (823 MPa) making it flexible.

Moreover, it is desirable to have circular polarization for many different applications where the alignment of the receiving and transmitting antenna may impact the overall performance of the system such as radars [23], satellite communications and on-body antenna system [21], [24], [25].

Presence of open stopbands (OSBs) also impacts the scanning of the antenna through the broadside direction [26], [27]. Several techniques have been proposed to suppress or completely mitigate OSBs [28–30]. At the OSB frequency, the input impedance matching is poor and the Bloch impedance (Z_s) has a high imaginary value. Hence, the aim is to minimize the high imaginary value of impedance to reduce the effects of OSB. The idea of beam scanning due to higher spatial harmonic, limited to a single-band and linear polarization, has been presented in [31] with no suppression of OSB.

In this paper, single-layer PCB meandering microstrip based LWA is proposed with dual-band operation without the use of vias shown in Fig 1(a). The Ku-band operation of the antenna

is due to the $n = -1$ spatial harmonic and it exhibits linear polarization, while the second band of operation at K-band is due to $n = -2$ and it depicts circular polarization as described in Fig. 1(b). The unit cell of the periodic antenna consists of three meanders to ensure single-beam operation by providing better separation between the different spatial harmonics.

The structure of the paper is as follows. Section II details the concept of higher spatial order in a microstrip-based unit cell followed by theoretical formulation for the dimensions required to have circular polarization for a unit cell with single meander. In Section III, the unit cell is modified by adding two smaller meanders to increase the separation of spatial harmonics and ameliorate performance of circular polarization over the larger frequency operation range. The smaller meanders also result in better control over scanning rate (i.e. the ratio between the change in the angle of maximum radiation and the change in frequency $\Delta\theta/\Delta f$). A technique to remove OSB is discussed using Bloch impedance subsequently. Section IV contains the comparison of simulations and measurements for the final design. In Section V, the conclusions of the study are presented.

II. RADIATION MECHANISM AND PRINCIPLE FOR ANTENNA DESIGN

Fig. 1(a) shows the design of the proposed microstrip-based LWA with mitred corners. As detailed in previous works on microstrip based LWAs [13], the radiation occurs due to the magnetic current at the corners of the meandering microstrip.

The evolution towards the final design of the unit cell is shown in Fig. 2. Conventional microstrip-based LWA [9], [13], [32-34] operate in the radiation zone due to spatial harmonic of $n = -1$ like the unit cell shown in Fig. 2(a). This unit cell can be modified to operate in the $n = -2$ spatial harmonic, by increasing the pathlength at the desired operational frequency. By introducing mitred corners and properly choosing the length of the interconnecting microstrip lines between the corners the antennas radiates in circular polarization (see Fig. 2(b)). The unit cell operates in the radiation zone associated with $n = -1$ and $n = -2$ spatial harmonics.

To improve the separation of radiation zone due to two harmonics ($n = -1, -2$) we propose the geometry in Fig. 2(c). The unit cell is modified with two additional meanders resulting in improvement in scanning range and circular polarization. The antenna has been optimized for operation in the circularly polarized K-band using the spatial harmonic of $n = -2$, and all theoretical formulations for the unit cell dimensions have been performed to ensure optimal performance in this frequency range.

A. Higher order spatial harmonics in the unit cell based on microstrip design

Fig. 3(c) shows the microstrip based unit cell with single meander with four radiating elements due to four mitred corners. Due to the periodicity (p_0) of the structure, infinite

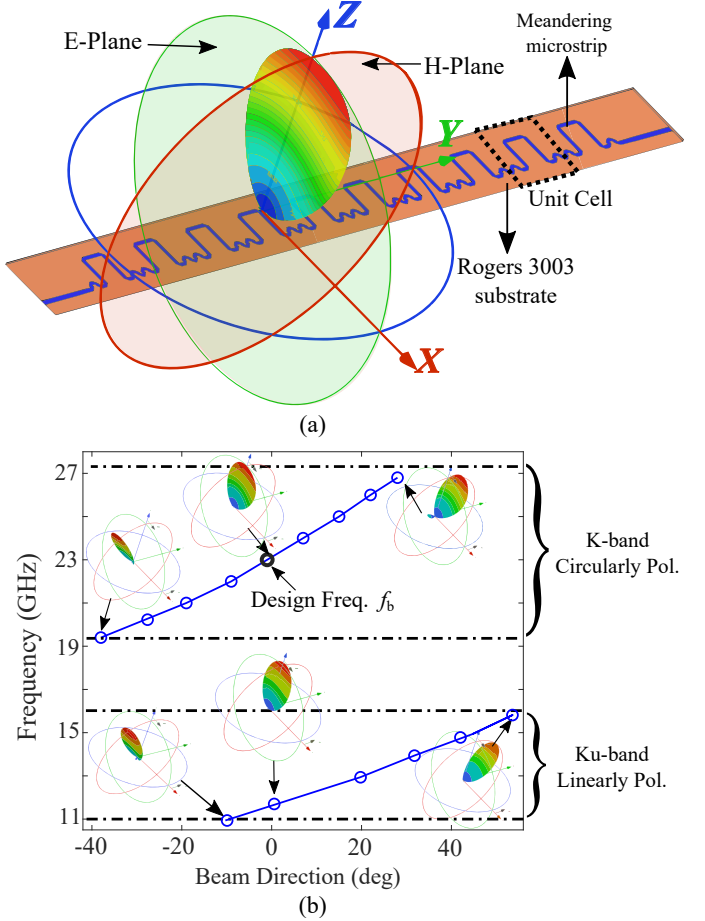


Fig. 1: (a) Configuration of the proposed 10 unit cells periodic frequency scanning antenna with radiation pattern shown in the broadside direction. The meandering microstrip is etched on top layer while bottom layer is copper. (b) Beam scanning operation of the proposed LWA as a function of frequency in the Ku-band and Ka-band. The antenna radiates a fan-beam in the E-plane (X-Z plane) while in the H-plane (Y-Z plane) the antenna changes the direction of maximum radiation with change in frequency.

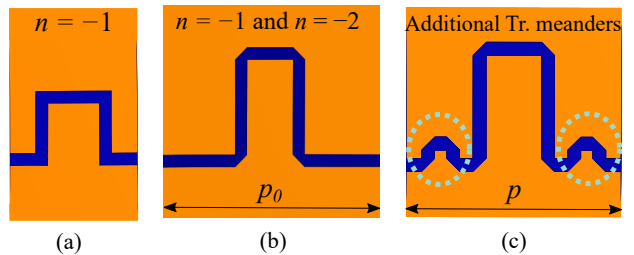


Fig. 2: Evolution towards final design of proposed unit cell: (a) conventional unit cell operating in single band and radiating due to the $n = -1$ spatial harmonic, (b) dual band operating unit cell radiating due to $n = -1$ and $n = -2$ spatial harmonics, and (c) modified unit cell with the introduction of two meanders ($p < p_0$) to improve the scanning range and the circular polarization performance.

number of space harmonics exist due to Bloch-Floquet theorem [35], [36]. The phase constant of the n^{th} space harmonic β_n satisfies

$$\beta_n p_0 = \beta_0 p_0 + 2n\pi \quad (1)$$

where n ranges from $-\infty$ to $+\infty$. Here β_0 is the zeroth order propagation constant in the microstrip medium.

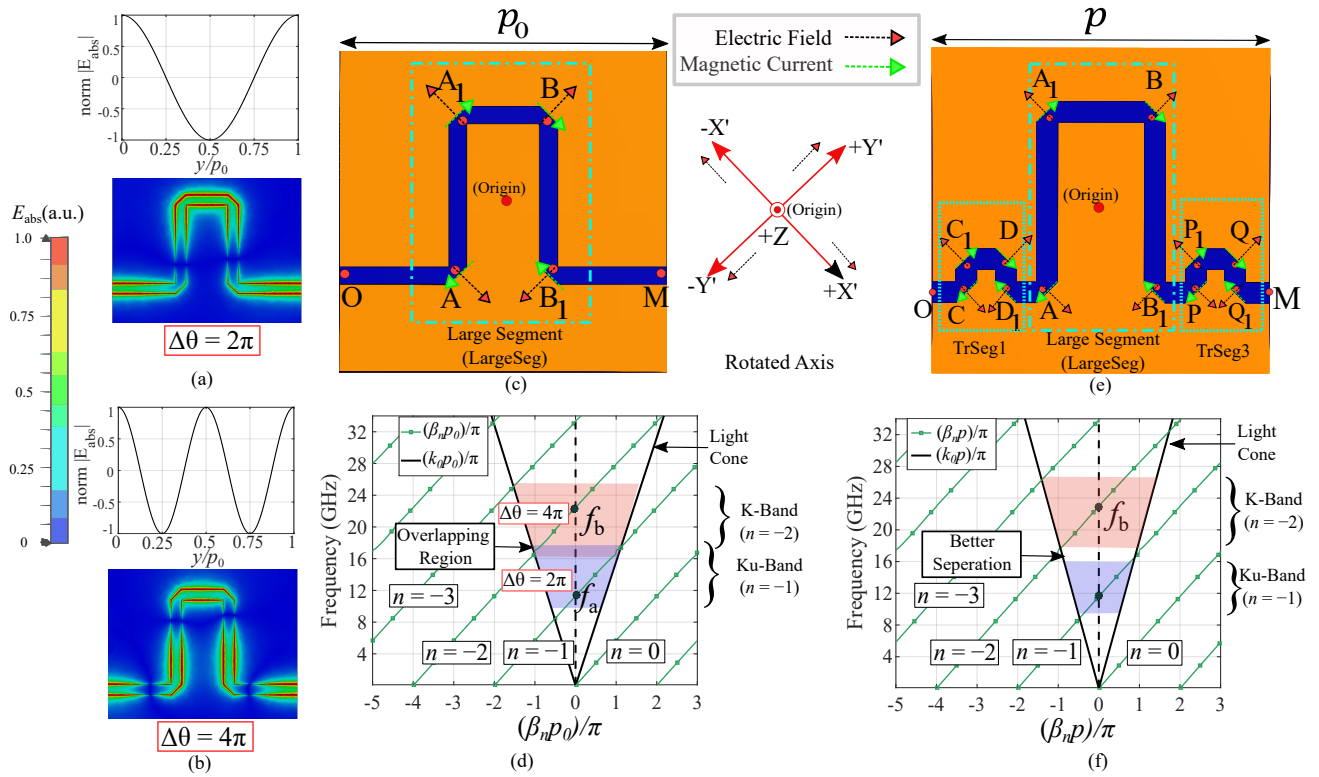


Fig. 3: E_{abs} plots at phase 0° for the frequency at which broadside radiation occurs for (a) $n = -1$ and (b) $n = -2$. The sinusoidal graphs above E_{abs} plots are representative of the electric field variation across microstrip line throughout the unit cell. (c) Unit cell with single large meander. Radiation sources for a single large meander are depicted in the figure. The four radiating magnetic current sources are shown at points A, A₁, B and B₁. (d) Brillouin diagram for the unit cell with the single meander. (e) Unit cell design with two additional meanders that results in 12 radiation sources. (f) Brillouin diagram for the improved unit cell with two additional meanders.

Fig. 3(d) shows the corresponding Brillouin diagram for the unit cell. The n^{th} spatial harmonic inside the light cone ($|\beta_n| < |k_0|$), results in radiation [15]. It is to be noted that multiple spatial harmonics can exist within the light cone resulting in multiple beam radiation [16].

From equation (1), the phase difference across the unit cell for the first two higher harmonics $n = -1$ and $n = -2$ (near the light cone) can be described in the following manner with respect to fundamental harmonic:

$$\beta_{-1}p_0 = -\pi \text{ to } \pi \rightarrow \beta_0p_0 = \pi \text{ to } 3\pi \quad (2a)$$

$$\beta_{-2}p_0 = -\pi \text{ to } \pi \rightarrow \beta_0p_0 = 3\pi \text{ to } 5\pi \quad (2b)$$

Likewise, the direction of maximum radiation θ_n corresponding to n^{th} spatial harmonic is given by [16], [36], [37]

$$\theta_n = \sin^{-1}(\beta_{-n}p_0/k_0p_0) \quad (3)$$

where k_0 is the free space wave number.

According to equation (3), when the phase difference across the unit cell ($\beta_{-n}p_0$) is zero, the direction of main beam of the n^{th} spatial harmonic is in the broadside direction. Hence, at the frequencies of broadside radiation for spatial harmonics $n = -1$ and $n = -2$, the phase difference across the unit cell from equation (1) is:

$$\beta_{-1}p_0|_{f=f_a} = 0 \rightarrow \beta_0p_0|_{f=f_a} = 2\pi \quad (4a)$$

$$\beta_{-2}p_0|_{f=f_b} = 0 \rightarrow \beta_0p_0|_{f=f_b} = 4\pi, \quad (4b)$$

where f_a and f_b are the frequencies corresponding to the broadside radiation for $n = -1$ and $n = -2$, respectively. Fig. 3(a-b) depicts the variation of electric field magnitude at the two frequencies confirming the above two equations. To summarize, the first Ku-band radiation is due to spatial harmonic $n = -1$, while the second K-band radiation is due to spatial harmonic $n = -2$.

Eq. (4b) implies that at $f = f_b$, the total phase difference (ϕ_{p_0}) across the unit cell is equal to 4π . Therefore, the equation to have broadside radiation for second harmonic at the design frequency $f = f_b$ is,

$$4\pi = \phi_{OA_1|f=f_b} + \phi_{AA_1|f=f_b} + \phi_{A_1B|f=f_b} + \phi_{BB_1|f=f_b} + \phi_{B_1P|f=f_b} \quad (5)$$

Here, ϕ_{ij} is the phase difference across the line segment between the points i and j , where $i, j \in \{A, A_1, B, B_1, O, M\}$. As indicated earlier, the reason for designing the antenna for the second harmonic is to obtain dual band operation due to spatial harmonics $n = -1$ and $n = -2$.

B. Analysis for circular polarization in the radiation zone for spatial harmonic $n = -2$

To analyse the circular polarization easily, the axis is rotated equal to the angle of mitred corners as shown in Fig.3(c). Hence there are two transverse components ($E_{X'}$ and $E_{Y'}$) radiating from the mitred corners.

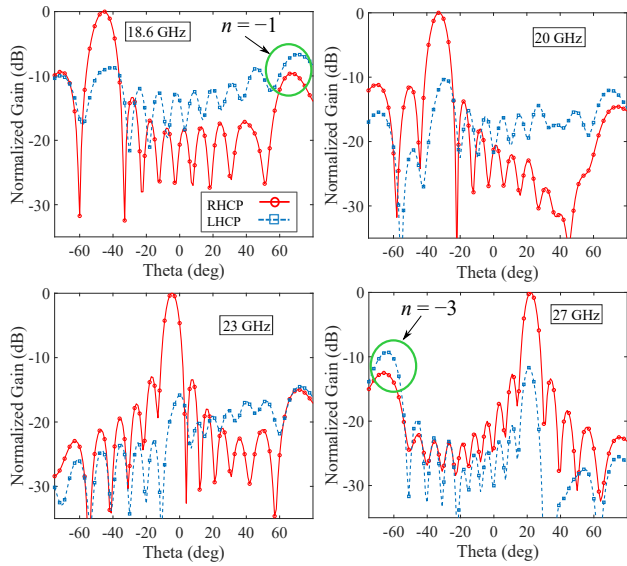


Fig. 4: Normalized RHCP and LHCP gain in the H-plane obtained from simulation for the LWA formed by connecting 10 unit cells with singular meander. The main lobe is due to spatial harmonic of $n = -2$. The realized gain of the main lobe varies from 8 dB to 14 dB across the frequency range.

The ratio of the two transverse fields, $E_{X'}$ and $E_{Y'}$ [14]:

$$\frac{E_{Y'}}{E_{X'}} = e^{\phi_{AA_1} + \phi_{A_1B}} = e^{-j\beta_0(l_{AA_1} + l_{A_1B})} \quad (6)$$

Additionally, l_{ij} represents the length of the line segment between the points i and j , which were indicated earlier. To have accurate length of line intervals, the model from [9] is chosen for analysis.

To have the circular polarization, the two transverse components of electric field ($E_{X'}$ and $E_{Y'}$) need to have a phase difference of odd multiple of $\pi/2$ [2]. Consequently, the condition to obtain circular polarization for a travelling-wave meandering microstrip antenna is stated by [14].

$$\phi_{AA_1} + \phi_{A_1B} = \beta_0(l_{AA_1} + l_{A_1B}) = (2k + 1)\pi/2 \quad (7)$$

where $k = 1, 2, \dots$

Since the desire is to operate in spatial harmonic of $n = -2$, from equation (2b) and (4b), the conclusion can be made to select $k = 1$, hence

$$\phi_{AA_1} + \phi_{A_1B} = 3\pi/2 \quad (8)$$

Selecting $k \geq 2$ would lead to similar result with equation (6) still being satisfied, however this would increase the overall period of the unit cell resulting in non desirable harmonics in the radiation zone.

Equation (8) imposes a criterion on the the phase difference and hence the length of microstrip interval between two corners A and B for achieving circular polarization. For initial dimensions, at the design frequency $f = f_b$, l_{AA_1} is taken such that $\phi_{AA_1} = \pi$. This implies that $\phi_{A_1B} = \pi/2$.

From Fig. 3(d), $l_{AA_1} = l_{BB_1}$ which implies $\phi_{AA_1} = \phi_{BB_1}$. Also, the unit cell is considered symmetric, hence $l_{OA} = l_{B_1M}$.

The phase difference across the large meander (consisting of AA_1 , A_1B and BB_1) is defined as $\phi_{LargeSeg}$. Therefore, from

TABLE I
DIMENSIONS OF THE UNIT CELL DESIGNED TO OPERATE IN SPATIAL HARMONIC OF $n = -2$ AND HAVE CIRCULARLY POLARIZED FIELDS. HERE NOTE THAT λ_b IS THE CORRESPONDING WAVELENGTH IN THE MICROSTRIP MEDIUM AT $f = f_b$

Line interval	Expressed in λ_b	Phase diff. across line interval	Physical dim. (mm)
OA	$3\lambda_b/8$	$3\pi/4$	3.21
AA ₁	$\lambda_b/2$	π	4.44
A ₁ B	$\lambda_b/4$	$\pi/2$	2.47
BB ₁	$\lambda_b/2$	π	4.44
B ₁ M	$3\lambda_b/8$	$3\pi/4$	3.21
p_0	$2\lambda_b$	4π	5.8
t_{50}	-	-	0.5
h_{sub}	-	-	0.254

equation (8), in order to have the best circular polarization performance at the desired design frequency of $f = f_b$,

$$\phi_{LargeSeg}|_{f=f_b} = \phi_{AA_1}|_{f=f_b} + \phi_{A_1B}|_{f=f_b} + \phi_{BB_1}|_{f=f_b} = 5\pi/2 \quad (9)$$

Consequently, there are two design constraints on the length of microstrip line intervals: 1) Equation (5), to construct a unit cell that has broadside radiation at $f = f_b$. and 2) Equation (9), to construct a unit cell with best circular polarization performance at $f = f_b$. Table I depicts the dimensions of the unit cell based on the theory discussed at $f_b = 23$ GHz. The dimensions are mentioned in the form of λ_b , corresponding wavelength to frequency f_b in the microstrip medium.

The dielectric is chosen as Rogers 3003 ($\epsilon_r = 3.0$) while the height of the substrate is $h_{sub} = 0.254$ mm. The width of the microstrip t_{50} is equal to 0.5 mm. It is important to note that in the microstrip medium the effective $\epsilon_{r,eff}(f = 0)$ is 2.375 calculated from [38]. To account for the dispersive nature of microstrip media, the model proposed by Pramanick and Bhartia from [39] is considered to calculate $\epsilon_{r,eff}(f = f_b)$. This parameters are taken into consideration when calculating λ_b in the microstrip medium.

Ten such unit cells with single meander are cascaded next to each other to form a LWA and full-wave simulations are performed in CST and ANSYS HFSS. Fig. 4 shows the radiation pattern indicating the beam scanning with frequency and circular polarization nature of the antenna. As can be seen, at lower end of frequency range $f = 18.6$ GHz, there is another beam of spatial harmonic of $n = -1$ limiting the scanning.

The corresponding axial ratio obtained through simulation at the angle of maximum gain is shown in Fig. 5(a). The antenna has good circular polarization performance near the design frequency of $f_b = 23$ GHz. The frequency range where the axial ratio is lower than 3 dB is from 20 GHz to 25.2 GHz with the beam scanning from $(-26^\circ$ to $+10^\circ$).

C. Improvement in the scanning range by reducing the period of the unit cell

In the previous subsection, initial dimensions were taken such that $\phi_{AA_1} = \pi$ and $\phi_{A_1B} = \pi/2$ at $f = f_b$. The scanning

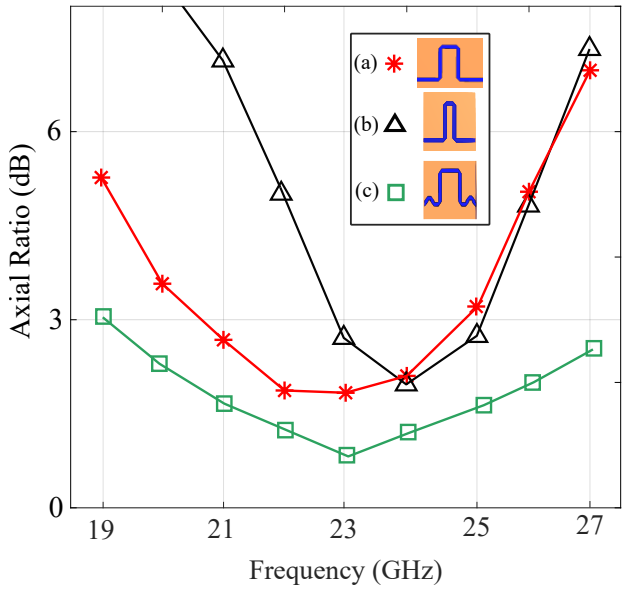


Fig. 5: Axial ratio values in the main beam direction versus frequency obtained by full-wave simulation of 10 unit cells connected in series for 3 cases: (a) Single meander with $\phi_{AA_1} = \pi$. (b) Single meander with $\phi_{AA_1} = 9\pi/8$ to reduce the period of the unit cell. (c) Two additional meanders on either side of large meander.

range and the separation of the harmonics can be increased by reducing the period of a unit cell. If the vertical length l_{AA_1} is increased such that $\phi_{AA_1} = 9\pi/8$, then according to (8), to maintain the circular polarization performance $\phi_{A_1B} = \pi/4$ at the design frequency f_b . This reduces the period of the unit cell since the horizontal interval (l_{A_1B}) of the unit cell is shortened leading to better separation of harmonics. The rest of the dimensions remain the same as discussed in Table I.

Ten such unit cells are connected in series to form a LWA and full-wave simulations are performed in CST and Ansys HFSS. However, as can be seen from Fig. 5(b), there is a negative impact on the circular polarization performance in the operating frequency band.

In both the discussed cases with only a single meander in the unit cell (see Fig. 5(a, b)), at the design frequency $f = f_b$ and in the frequency range close to it, the antenna shows good circular polarization performance. However, it deteriorates quite fast towards the lower and higher end of frequencies. Hence, the beam scanning range is pretty limited.

It can be concluded that using a unit cell with only a single large meander, is extremely challenging and not feasible to obtain large beam scanning range with good circular polarization performance.

III. IMPROVEMENT IN THE SCANNING RANGE AND CIRCULAR POLARIZATION BY ADDITIONAL MEANDERS

To enhance the beam steering range, improve circular polarization performance across the operational frequency band, and gain better control over scanning rate ($\Delta\theta/\Delta f$), two additional smaller meanders are introduced on either side of larger meander at an equal distance. The following sections describe the characteristics and steps to design such a unit cell.

A. Constructing the unit cell with three meanders for dual-band operation

Fig.3(e) depicts the design of improved unit cell. The first additional meander consists of three microstrip line intervals CC_1 , C_1D and DD_1 , while the third additional meander consists of line intervals PP_1 , P_1Q and QQ_1 . The lengths of each of these 6 microstrip line intervals is equal. The phase difference across these three microstrip line interval is defined to be ϕ_{sect} . Additionally, phase difference due to the first and the third meander is denoted by ϕ_{TrSeg1} and ϕ_{TrSeg3} .

The unit cell is designed to be symmetric, therefore the phase difference across the line intervals is $\phi_{D_1A} = \phi_{B_1P}$, $\phi_{OC} = \phi_{Q_1M}$, and $\phi_{\text{TrSeg1}} = \phi_{\text{TrSeg3}}$. Furthermore, the phase difference across the 1st meander and the 3rd meander can be written as

$$\phi_{\text{TrSeg1}} = \phi_{CC_1} + \phi_{C_1D} + \phi_{DD_1} = 3 \times \phi_{\text{sect}} \quad (10a)$$

$$\phi_{\text{TrSeg3}} = \phi_{PP_1} + \phi_{P_1Q} + \phi_{QQ_1} = 3 \times \phi_{\text{sect}} \quad (10b)$$

In order to have broadside radiation at frequency of $f = f_b$, equation (4b) (for this unit cell with period p , the equation is $\beta_0 p = 4\pi$) must be satisfied. Consequently, from the Fig. 3(e), the design equation for the improved unit cell can be written as:

$$4\pi = \phi_{OC}|_{f=f_b} + \phi_{\text{TrSeg1}}|_{f=f_b} + \phi_{D_1A}|_{f=f_b} + \phi_{\text{LargeSeg}}|_{f=f_b} + \phi_{B_1P}|_{f=f_b} + \phi_{\text{TrSeg3}}|_{f=f_b} + \phi_{Q_1M}|_{f=f_b} \quad (11)$$

Here, ϕ_{ij} represents the phase difference between the points i and j where $i, j \in \{C, C_1, D, D_1, A, A_1, B, B_1, P, P_1, Q, Q_1, O, M\}$.

To maintain circular polarization, it is necessary that phase difference across larger meander $\phi_{\text{LargeSeg}}|_{f=f_b}$ equals $5\pi/2$, as stated in equation (9). Therefore, the following design constraint can be derived from equation (11):

$$6 \times \phi_{\text{sect}}|_{f=f_b} + 2 \times \phi_{D_1A}|_{f=f_b} + 2 \times \phi_{OC}|_{f=f_b} = 3\pi/2 \quad (12)$$

B. Circular polarization analysis for the improved unit cell

It was proved in Section II that a single meander unit with four radiating elements can produce circular polarization at the desired design frequency. Hence, for the improved unit cell with 12 radiating currents (see Fig. 3(e)), circular polarization at $f = f_b$ can be achieved if the effect due to radiating currents on the first additional meander (at C, C_1, D and D_1) and the third additional meander (at P, P_1, Q and Q_1) is nullified. This is possible if the direction of current at C is opposite to the current at P resulting in opposing fields at these corners.

The magnetic currents at the corners C and P are oriented along the Y' axis as shown in Fig. 1(b), but depending on the phase shift introduced by the interconnecting microstrip lines, they can have the same or opposite directions. Hence, the length of the microstrip line intervals in between these two corners can be optimized in such a way that the magnetic currents are in opposite direction at design frequency $f = f_b$.

The direction of magnetic current at C will be opposite to the magnetic current at P if the following constraint is met at $f = f_b$ (since $e^{3\pi} = -1$):

$$\phi_{OP} - \phi_{OC} = 3\pi \quad (13a)$$

$$\phi_{TrSeg1} + \phi_{D1A} + \phi_{LargeSeg} + \phi_{B1P} = 3\pi \quad (13b)$$

From equation (9), it is known that to maintain circular polarization at $f = f_b$, $\phi_{LargeSeg} = 5\pi/2$, hence the following design equation is obtained

$$3 \times \phi_{sect}|_{f=f_b} + 2 \times \phi_{D1A}|_{f=f_b} = \pi/2 \quad (14)$$

The equations (9), (12) and (14) are the design constraints on the length of line intervals for the proposed unit cell to maintain broadside radiation and circular polarization at $f = f_b$.

From equation (9), it is clear that the dimensions for larger meander are fixed to maintain circular polarization. The other dimensions are governed by equations (12) and (14). This results in 3 variables (namely $\phi_{sect}|_{f=f_b}$, $\phi_{D1A}|_{f=f_b}$ and $\phi_{OC}|_{f=f_b}$) and 2 equations. In the current analysis $\phi_{sect}|_{f=f_b}$ is considered an independent variable making the other two variables ($\phi_{D1A}|_{f=f_b}$ and $\phi_{OC}|_{f=f_b}$) dependent. Initial design is chosen such that $\phi_{sect}|_{f=f_b} = 10^\circ$. The other two dimensions can hence be calculated from equation (12) and equation (14). The initial lengths of the microstrip sections following this theory are shown in the table II for $f_b = 23$ GHz.

Fig. 6 shows the full-wave simulation of the unit cell at $f = f_b$ designed according to the equations above. As can be seen the direction of fields at each of the corners in the 1st smaller meander is opposite to the field at the corresponding corner of the 3rd smaller meander.

10 such unit cells are sequentially connected as shown in Fig. 1(b) to form a LWA and then simulated in CST. Fig. 5(c) shows the unit cell (in the inset) designed by the formulated theory described above and simulation respectively, of axial ratio obtained for different frequencies over the scanning range for the main fan beam direction emanated from the LWA. Notable improvement in axial ratio performance over a larger frequency band can be observed following the inclusion of two smaller meanders.

C. Performance improvement due to the two additional meanders

Due to the two additional smaller meanders the electrical length of the unit cell has been increased. This results in following improvements for frequency scanning:

- enhanced scanning range,
- better control over scanning rate by dictating the size of path-length in the unit cell by reducing or increasing the size of small meanders (ϕ_{sect}),
- better separation of spatial harmonics resulting in lower sidelobes due to non-desired spatial harmonics,
- improvement of circular polarization performance across the band.

By comparing the Brillouin diagrams in Fig. 3(c) and Fig. 3(e) for the unit cell geometry containing one meander and three meanders, respectively, the first three conclusions

TABLE II
DIMENSIONS OF THE UNIT CELL WITH 3 MEANDERS DESIGNED TO OPERATE IN SPATIAL HARMONIC OF $n = -2$ AND HAVE CIRCULARLY POLARIZED FIELDS. NOTE THAT λ_b IS WAVELENGTH CORRESPONDING TO f_b IN MICROSTRIP MEDIUM

Line interval	Initial Values (From the theory)		Optimised (mm)
	Expressed in λ_b	(mm)	
CC ₁ =C ₁ D=DD ₁	$\phi_{sect} \times (\lambda_b/2\pi)$	0.71	0.745
D ₁ A=B ₁ P	$(\pi/2 - 3\phi_{sect})/2 \times (\lambda_b/2\pi)$	1.128	1.172
AA ₁	$\lambda_b/2$	4.265	4.343
A ₁ B	$\lambda_b/4$	2.383	3.062
BB ₁	$\lambda_b/2$	4.265	4.343
PP ₁ =P ₁ Q=QQ ₁	$\phi_{sect} \times (\lambda_b/2\pi)$	0.71	0.745
OC=Q ₁ M	$(\pi - 3\phi_{sect})/2 \times (\lambda_b/2\pi)$	1.819	0.376
p	$2 \times \lambda_b$	9.694	8.028
t_{50}	-	0.5	0.5
h_{sub}	-	0.254	0.254

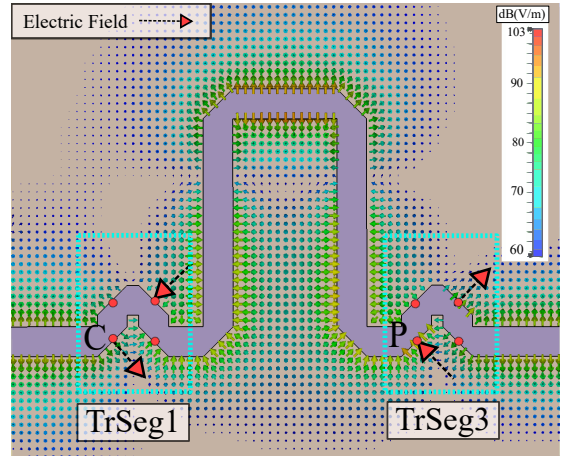


Fig. 6: Full-wave simulation for the unit cell constructed using the theoretical formulation. At $f = f_b$, the electric fields at each of the four mitred corners of TrSeg1 cancels out with corresponding mitred corner of TrSeg3.

can be easily drawn. With the help of additional two meanders the rate of dispersion with frequency is controlled within the unit cell. The impact of the proposed geometry on the circular polarization can be observed from Fig. 5. The acceptable range for frequency scanning (frequency range where axial ratio < 3 dB) has increased from 20 GHz to 25.2 GHz to 19.4 GHz to 27.5 GHz resulting in increase of beam steering from $(-26^\circ$ to $+10^\circ)$ to $(-42^\circ$ to $+30^\circ)$. The beam steering $(-42^\circ$ to $+30^\circ)$ is discussed in Section IV.

D. Mitigation of OSB

Periodic structures like LWAs have a frequency band near the broadside frequency (f_b in current case), where there is no conduction of the travelling-wave, known as OSB [2], [15]. To remove OSB, the parameter of Bloch impedance (Z_s) has to be analysed. The Bloch impedance can be calculated from the S-parameters extracted from driven-mode full-wave simulation

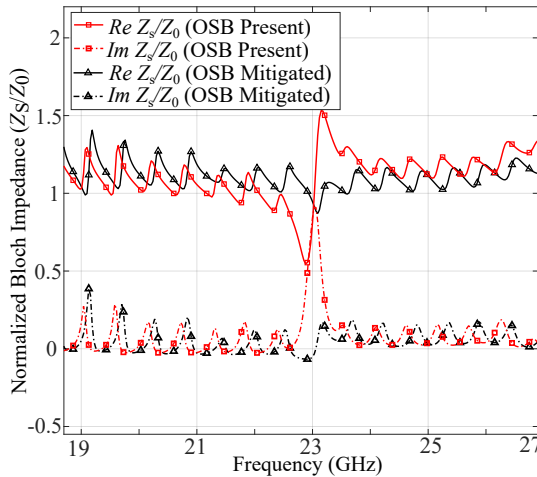


Fig. 7: The Bloch impedance of the LWA when OSB is present and when OSB is mitigated by the introduction of additional capacitance. Here the impedance is normalised to $Z_0 = 50\Omega$.

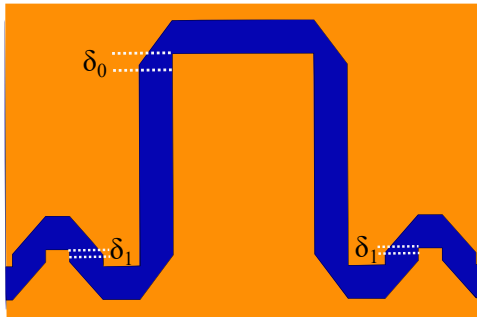


Fig. 8: OSB mitigation by changing the angle of mitred corner. The values of δ_0 and δ_1 are 0.15 mm and 0.06 mm respectively.

in terms of circuit parameters A, B, C and D as shown in [38]:

$$Z_s = \frac{-2 \times B}{(A - D - \sqrt{(A + D)^2 - 4})} \quad (15)$$

Fig. 7 shows the Bloch impedance extracted for the K-band operation range. For the case when OSB is present, at the broadside frequency, $f_b = 23$ GHz, there is an abrupt increase in imaginary Z_s , which results in poor transmission and high return loss. This results in reduced gain at the broadside region.

To mitigate the problem of OSB, a technique similar to [13] is employed. For a meandering microstrip with mitred corners the effect of bending the microstrip line (corners) can be modelled as capacitance [40-42]. This is clearly evident from Fig. 7 when OSB is present. Hence, the angle for the mitred corners are changed which introduces an additional inductance [41], [42] that reduces imaginary impedance at $f = f_b$ as shown in Fig. 8. Fig. 7 shows that imaginary impedance goes to zero which leads to mitigation of OSB at broadside direction.

IV. DUAL-BAND LEAKY-WAVE ANTENNA

A 10 unit cell dual band LWA, having the layout of Fig. 1(b) and the optimised dimensions listed in Table II was fabricated. The antenna is based on Rogers 3003 ($\epsilon_r = 3.0$ and $\tan \delta = 0.001$) with a substrate thickness of 0.254 mm.

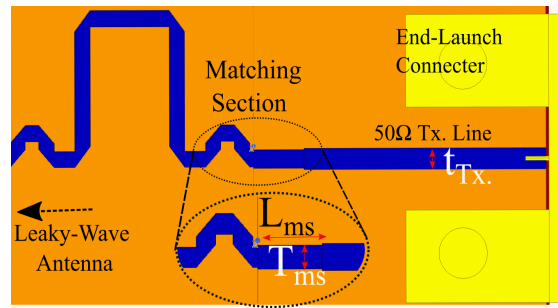


Fig. 9: Feed Design to match the output impedance (Z_0) of 50Ω connector to input impedance of of antenna at around 60Ω . The values for matching section is $T_{ms} = 0.57$ mm and $L_{ms} = 1.634$ mm. The 50Ω transmission line is $t_{Tx} = 0.64$ mm.

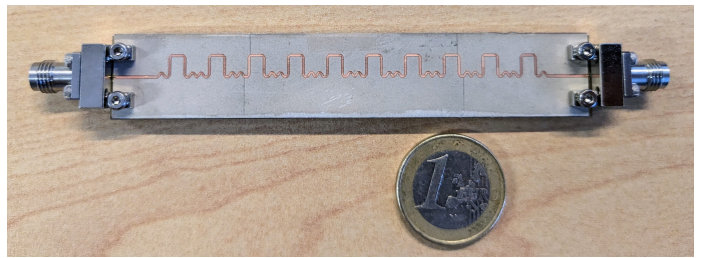


Fig. 10: Fabricated Leaky-Wave Antenna.

A. Feed design

A Bulgin end-launch connector (2.4 mm) with the output impedance $Z_0 = 50 \Omega$ is used to feed the antenna. The Z_s of the antenna is around 60Ω throughout the operating frequency range as shown in Fig. 7. Hence a matching section is added to match the impedance depicted in Fig. 9.

B. Circularly polarized radiation in K-band

In this band, the antenna is right-handed circularly polarized and radiation is due to spatial harmonic of $n = -2$. The measurements are performed at the millimeter-wave test facility CAMILL at Institut d'Électronique et de Télécommunications de Rennes (IETR). The simulated and measured radiation pattern in the azimuth plane are shown in Fig. 11(a-d) for the 19.4 GHz to 27.5 GHz band. The measured radiation pattern at $f = 19.4$ GHz shows higher side-lobes compared to simulations. This is due to the fact that there is reflection from the connector due to a very tilted beam in the H-plane. The 3-dB beamwidth of the antenna is about 10° throughout the operational range. The length of the antenna remains compact at $7.67\lambda_0$.

The efficiency of the antenna in this band varies from 0.5 to 0.75. Measured and simulated axial ratio are compared in Fig. 11(e). The realized gain plot of the reconfigurable fan-beam radiation pattern in the H-plane is also shown in Fig. 11(e). The measured S-parameters show that the reflection coefficient remains below -10 dB for the operational range.

C. Linearly polarized radiation in Ku-band

The antenna behaves as a linearly polarized antenna in the Ku-band 11 GHz to 15.5 GHz and the radiation occurs

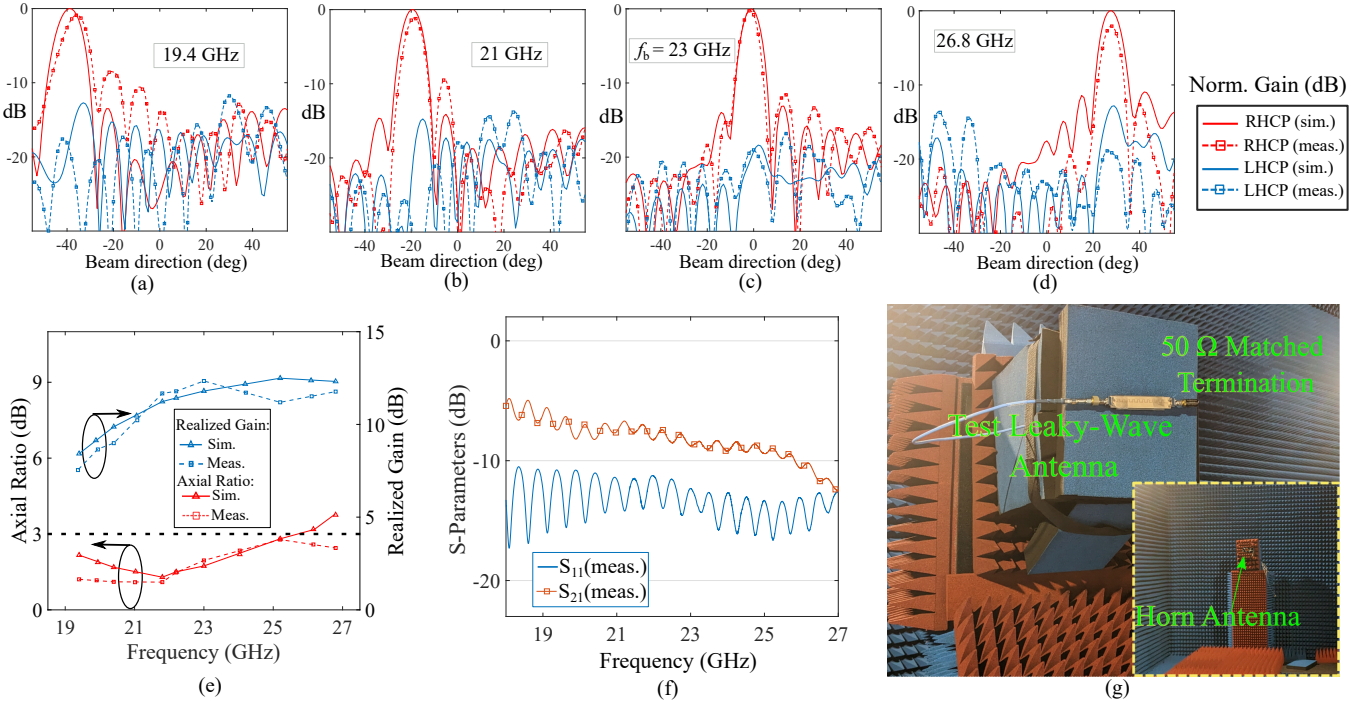


Fig. 11: Measurements in K-band where the antenna is circularly polarized. The measured and simulated normalized radiation pattern of the fabricated antenna in the H-Plane for (a) $f = 19.4$ GHz. (b) $f = 21$ GHz. (c) $f = 23$ GHz. (d) $f = 26.8$ GHz. The antenna scans from -42° to 30° in the K-band frequency range. (e) The axial ratio of the fabricated antenna remains below 3 dB throughout the operational frequency range. The measured realized gain of the antenna in the H-Plane ranges from 8 dB to 13.8 dB. (f) Measured transmission and return loss parameters. (g) Measurement setup of the antenna.

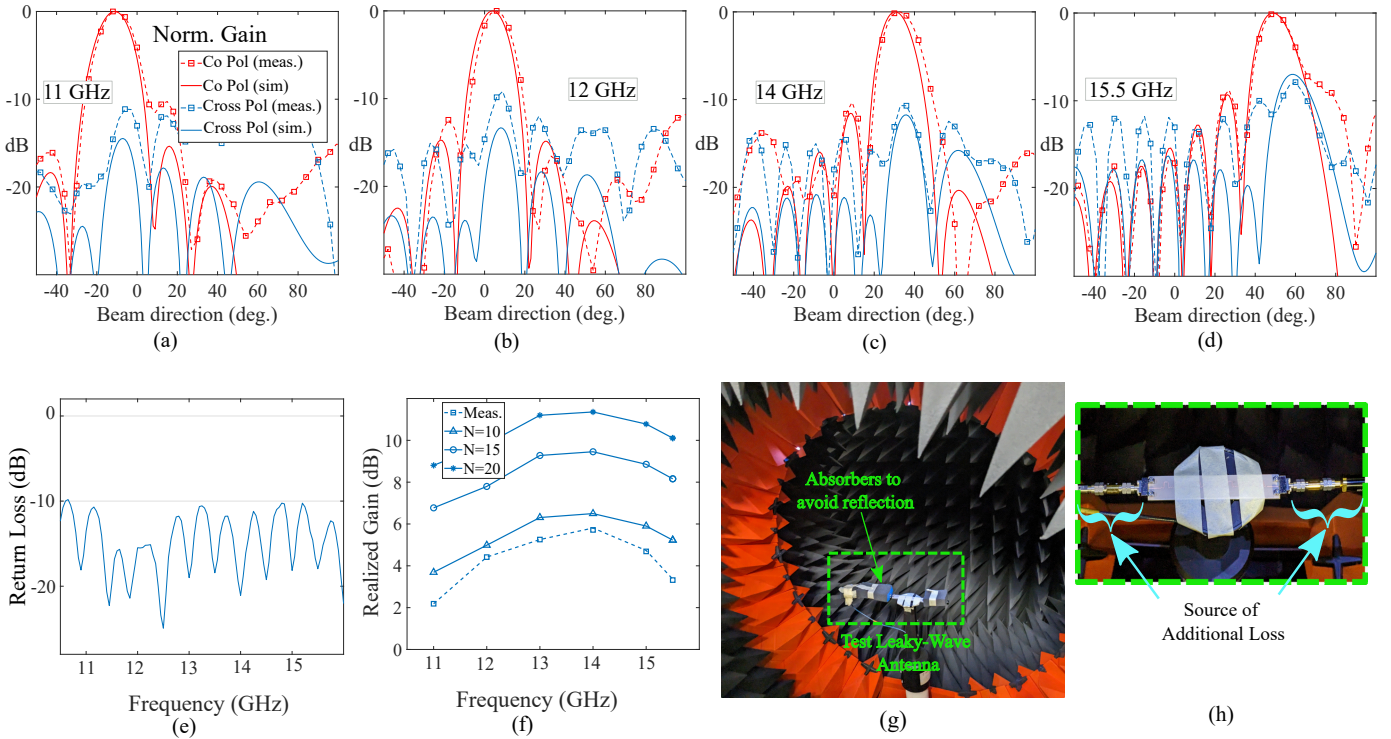


Fig. 12: Measurements in the Ku-band where the antenna depicts linear polarization. The measured normalized radiation pattern pattern closely follows the radiation pattern predicted by the simulation for the frequencies (a) $f = 11$ GHz. (b) $f = 12$ GHz. (c) $f = 14$ GHz. (d) $f = 15.5$ GHz. (e) Measured return loss. (f) Realized gain in Ku-band with different number of unit cells obtained through full-wave simulations. (g) Experimental setup for the measurement in Ku-band. (h) The additional connectors required to connect the antenna to the ports of VNA.

TABLE III
COMPARISON WITH OTHER SCANNING LWAS OPERATING IN SIMILAR FREQUENCY RANGES

Ref	Antenna Type	Frequency BW	Scanning Range	Realized Gain (dB)	Rel. Permittivity (ϵ_r)	Pol.
[29]	Microstrip with metallized vias	20 GHz to 29 GHz	95° (−50° to 45°)	Approx. 10	6.15	Circular
[10]	Microstrip with metallized vias	9.8 GHz to 15 GHz	72° (−52° to 20°)	10.0–15.1	2.2	Circular
[43]	SIW	26 GHz to 43 GHz	70° (−40° to 30°)	13.4–15	3.0	Linear
[28]	SIW	23 GHz to 25 GHz	30° (−15° to 15°)	15	3.66	Circular
[44]	SIW	10 GHz to 14 GHz	65° (−40° to 25°)	5.1–13	3.0	Circular
[31]	Microstrip	20.6 GHz to 24.6 GHz	85° (−40° to 45°)	9.8–13	3.0	Linear
This Work – K-band	Microstrip	19.4 GHz to 27.5 GHz	72° (−42° to 30°)	7–13	3.0	Circular
This Work – Ku-band	Microstrip	11 GHz to 15.5 GHz	75° (−15° to 60°)	2.5–5	3.0	Linear

due to the spatial harmonic of $n = -1$. The simulated and measured realized gain are shown in Fig. 12(a)–(d). The antenna scanning range is of -15° to 60° . The 3-dB beamwidth of the antenna is less than 17° throughout the operational range. The measured reflection coefficient is below -10 dB in the operating frequency range as shown in Fig. 12(e).

Measurement is performed using MVG Starlab measurement system at IETR, as shown in Fig. 12(g). The antenna is fixed on the platform using tapes to avoid displacement. To avoid the elevated side-lobe levels at high tilted angles absorbers are added at the either end.

It has to be noted that the antenna has been designed to operate in K-band and Ku-band, with a special attention to the performance in K-band. As a consequence, the gain in Ku-band is limited to 5 dB. However, the realized gain can be improved by adding unit cells to the LWA as shown in Fig. 12(f). It is also important to notice that the realized gain in the Ku-band of the antenna is lower by 1–2 dB in the measurements than simulations as shown in Fig. 12(f). This is the effect of the connectors required to properly connect the antenna to the ports of Vector Network Analyzer (VNA) as depicted in Fig. 12(h).

D. Literature comparison

Table III shows the comparison with the antennas operating in similar frequency ranges along with fabrication technology. Circularly polarized LWAs operating in the range 9.8 GHz to 15 GHz and 20 GHz to 29 GHz based on microstrip are reported in [10], [29]. Both designs require via-holes, thus increasing the complexity for fabrication compared to the proposed design. Ref. [31], [45] report LWA based on microstrip operating in similar mm-Wave range however they exhibit linear polarization. Composite right left-handed (CRLH) based structures such as the ones reported in [3], [5], [46] are extremely sensitive to dimensions of the slot making them difficult to fabricate with precision at high frequencies.

Meanwhile, the proposed antenna achieves large beam scanning angles with simple meandering microstrips, while maintaining circular polarization. The design can be scaled at lower or higher frequencies very easily without the increase in complexity of fabrication.

V. CONCLUSION

This paper presents a novel approach to designing a compact and single-layer circularly polarized LWA. The approach is based on utilizing the time delay of microstrip line intervals to achieve circular polarization. The frequency scanning LWA operates as circularly polarized antenna in the K-band and as linearly polarized antenna in the Ku-band. This is possible by the use of spatial harmonics $n = -2$ and $n = -1$, respectively. To improve the band-separation and reduce the side-lobes due to unwanted harmonics in the radiation zone, additional meanders have been introduced. The axial ratio remains below 3 dB over large frequency range (19.4 GHz to 27.5 GHz) in the intended band for circular polarization. This ensures large scanning range from 72° (-42° to 30°). A novel technique to remove OSB is also explained in the work in order to have continuous scanning through broadside direction.

The proposed antenna does not make use of metallized vias hence significantly reducing the complexity of fabrication while maintaining compact size ($7.67\lambda_0$). The antenna is manufactured on a flexible substrate of Rogers 3003, making it suitable for flexible and conformal purposes at mm-wave frequencies.

REFERENCES

- [1] C. H. Walter, *Traveling Wave Antennas*. New York: McGraw-Hill, 1965.
- [2] C. A. Balanis, *Antenna Theory: Analysis and Design*. John Wiley & Sons, Dec. 2015.
- [3] R. Agarwal, R. L. Yadava, and S. Das, “A multilayered siw-based circularly polarized CRLH leaky wave antenna,” *IEEE Trans. Antennas Propag.*, vol. 69, no. 10, p. 10, May 2021.
- [4] A. Sarkar and S. Lim, “60 GHz compact larger beam scanning range PCB leaky-wave antenna using HMSIW for millimeter-wave applications,” *IEEE Trans. Antennas Propag.*, vol. 68, no. 8, pp. 5816–5826, Aug. 2020.
- [5] M. M. Sabahi, A. A. Heidari, and M. Movahhedi, “A compact CRLH circularly polarized leaky-wave antenna based on substrate-integrated waveguide,” *IEEE Trans. Antennas Propag.*, vol. 66, no. 9, pp. 4407–4414, Sep. 2018.
- [6] C. Caloz, T. Itoh, and A. Rennings, “CRLH metamaterial leaky-wave and resonant antennas,” *IEEE Antennas Propag. Mag.*, vol. 50, no. 5, pp. 25–39, Oct. 2008.
- [7] J. Liu, X. Tang, Y. Li, and Y. Long, “Substrate integrated waveguide leaky-wave antenna with H-shaped slots,” *IEEE Trans. Antennas Propag.*, vol. 60, no. 8, p. 6, May 2012.

- [8] G. P. Carrara, C. L. Zekios, and S. V. Georgakopoulos, "A TM11 high-order mode leaky wave antenna," *IEEE Trans. Antennas Propag.*, vol. 71, no. 1, pp. 119–130, Jan. 2023.
- [9] G. Sacco, O. Caytan, S. Pisa, and H. J. Visser, "Analysis and modelling of rampart line antennas," *IET Microw., Antennas Propag.*, vol. 15, no. 12, pp. 1605–1617, 2021.
- [10] S. Zhao and Y. Dong, "Circularly polarized beam-steering microstrip leaky-wave antenna based on coplanar polarizers," *IEEE Antennas Wireless Propag. Lett.*, vol. 21, no. 11, pp. 2259–2263, Nov. 2022.
- [11] N. Yang, C. Caloz, and K. Wu, "Full-space scanning periodic phase-reversal leaky-wave antenna," *IEEE Trans. Microw. Theory Techn.*, vol. 58, no. 10, pp. 2619–2632, Oct. 2010.
- [12] J. Duan and L. Zhu, "A transversal single-beam EH0-mode microstrip leaky-wave antenna on coupled microstrip lines under differential operation," *IEEE Antennas Wireless Propag. Lett.*, vol. 20, no. 4, pp. 592–596, Apr. 2021.
- [13] H. Wang, S. Sun, and X. Xue, "A periodic meandering microstrip line leaky-wave antenna with consistent gain and wide-angle beam scanning," *Int. J. RF Microw. Comput.-Aided Eng.*, vol. 32, no. 7, p. e23162, 2022.
- [14] J. R. James, P. S. Hall, and C. Wood, *Microstrip Antenna: Theory and Design*, ser. (IEE Electromagnetic Waves Series, No.12). London: IET ch 7, sec 7.4.1, pp. 215–218, 1986.
- [15] J. L. Volakis, *Antenna Engineering Handbook, Fourth Edition*. McGraw-Hill Education, 2007.
- [16] M. R. Rahimi, M. S. Sharawi, and K. Wu, "Higher-order space harmonics in substrate integrated waveguide leaky-wave antennas," *IEEE Trans. Antennas Propag.*, vol. 69, no. 8, pp. 4332–4346, Aug. 2021.
- [17] D.-F. Guan, Q. Zhang, P. You, Z.-B. Yang, Y. Zhou, and S.-W. Yong, "Scanning rate enhancement of leaky-wave antennas using slow-wave substrate integrated waveguide structure," *IEEE Trans. Antennas Propag.*, vol. 66, no. 7, pp. 3747–3751, Jul. 2018.
- [18] P. J. Soh, S. J. Boyes, G. Vandenbosch, Y. Huang, and a. S. L. Ooi, "On-body characterization of dual-band all-textile PIFA," *Progress In Electromagnetics Research*, vol. 129, pp. 517–539, 2012.
- [19] P. J. Soh, G. A. Vandenbosch, M. Mercuri, and D. M.-P. Schreurs, "Wearable wireless health monitoring: Current developments, challenges, and future trends," *IEEE Microw. Mag.*, vol. 16, no. 4, pp. 55–70, May 2015.
- [20] N. Chahat, M. Zhadobov, R. Sauleau, and K. Ito, "A compact UWB antenna for on-body applications," *IEEE Trans. Antennas Propag.*, vol. 59, no. 4, pp. 1123–1131, Apr. 2011.
- [21] I. V. Soares, P. Vadher, A. K. Skrivervik, G. Sacco, and D. Nikolayev, "Analysis of non-canonical body-conformal arrays with polarization decomposition," in *Proc. 17th Eur. Conf Antennas and Propag. (EuCAP 2023)*, Florence, Italy, Mar. 2023.
- [22] X. Tian, Q. Zeng, D. Nikolayev, and J. S. Ho, "Conformal propagation and near-omnidirectional radiation with surface plasmonic clothing," *IEEE Trans. Antennas Propag.*, vol. 68, no. 11, pp. 7309–7319, Nov. 2020.
- [23] J. Hasch, E. Topak, R. Schnabel, T. Zwick, R. Weigel, and C. Waldschmidt, "Millimeter-wave technology for automotive radar sensors in the 77 GHz frequency band," *IEEE Trans. Microw. Theory Techn.*, vol. 60, no. 3, pp. 845–860, Mar. 2012.
- [24] J. C. G. Matthews and G. Pettitt, "Development of flexible, wearable antennas," in *Proc. 3rd Eur. Conf. Antennas Propag. (EuCAP)*, Mar. 2009, pp. 273–277.
- [25] P. Vadher, G. Sacco, and D. Nikolayev, "On-body V-band leaky-wave antenna for navigation and safety applications," in *IEEE Microwaves, Antennas, and Propag. Conf. (MAPCon)*, Bangalore, Dec. 2022, pp. 1741–1746.
- [26] R. Henry and M. Okoniewski, "A broadside-scanning half-mode substrate integrated waveguide periodic leaky-wave antenna," *IEEE Antennas Wireless Propag. Lett.*, vol. 15, pp. 602–605, 2016.
- [27] D. R. Jackson and A. A. Oliner, "Leaky-Wave Antennas," in *Modern Antenna Handbook*. John Wiley & Sons, Ltd, 2008, pp. 325–367.
- [28] S. Otto, Z. Chen, A. Al-Bassam, A. Rennings, K. Solbach, and C. Caloz, "Circular polarization of periodic leaky-wave antennas with axial asymmetry: Theoretical proof and experimental demonstration," *IEEE Trans. Antennas Propag.*, vol. 62, no. 4, pp. 1817–1829, Apr. 2014.
- [29] M. H. Rahmani and D. Deslandes, "Backward to forward scanning periodic leaky-wave antenna with wide scanning range," *IEEE Trans. Antennas Propag.*, vol. 65, no. 7, pp. 3326–3335, Jul. 2017.
- [30] S. Paulotto, P. Baccarelli, F. Frezza, and D. R. Jackson, "A novel technique for open-stopband suppression in 1-D periodic printed leaky-wave antennas," *IEEE Trans. Antennas Propag.*, vol. 57, no. 7, pp. 1894–1906, Jul. 2009.
- [31] P. Vadher, G. Sacco, and D. Nikolayev, "Higher spatial harmonic leaky wave antenna design based on meandering microstrips," in *Proc. 17th Eur. Conf Antennas and Propag. (EuCAP)*, Florence, Italy, Mar. 2023.
- [32] S. Cheng, Y. Li, Z. Liang, S. Zheng, and Y. Long, "An approximate circuit model to analyze microstrip rampart line in osb suppressing," *IEEE Access*, vol. 7, pp. 90412–90417, 2019.
- [33] S.-L. Chen, D. K. Karmokar, Z. Li, P.-Y. Qin, R. W. Ziolkowski, and Y. J. Guo, "Circular-polarized substrate-integrated-waveguide leaky-wave antenna with wide-angle and consistent-gain continuous-beam scanning," *IEEE Trans. Antennas Propag.*, vol. 67, no. 7, pp. 4418–4428, Jul. 2019.
- [34] C. Wood, "Curved microstrip lines as compact wideband circularly polarised antennas," *IEE J. Microw. Opt. Acoust.*, vol. 3, no. 1, p. 5, 1979.
- [35] D. R. Jackson, C. Caloz, and T. Itoh, "Leaky-Wave Antennas," *Proceedings of the IEEE*, vol. 100, pp. 2194–2206, 2011.
- [36] R. E. Collin and F. J. Zucker, *Antenna Theory*. New York: McGraw-Hill, 1969, vol. 2, ch. 19-20.
- [37] A. Ishimaru, *Electromagnetic Wave Propagation, Radiation, and Scattering: From Fundamentals to Applications*, 2nd ed., ser. The IEEE Press Series on Electromagnetic Wave Theory. Piscataway, NJ: IEEE Press/Wiley, 2017.
- [38] D. M. Pozar, *Microwave Engineering*, 4th ed. Hoboken, NJ: Wiley, Nov. 2011.
- [39] M. Sadiku, S. Musa, and S. R. Nelatury, "Comparison of Dispersion Formulas for Microstrip Lines," in *IEEE SoutheastCon, 2004. Proceedings.*, Mar. 2004, pp. 378–382.
- [40] R. Douville and D. James, "Experimental study of symmetric microstrip bends and their compensation," *IEEE Trans. Microw. Theory Techn.*, vol. 26, no. 3, pp. 175–182, Mar. 1978.
- [41] P. Silvester and P. Benedek, "Microstrip discontinuity capacitances for right-angle bends, T junctions, and crossings," *IEEE Trans. Microw. Theory Techn.*, vol. 21, no. 5, pp. 341–346, May 1973.
- [42] P. Anders and F. Arndt, "Microstrip discontinuity capacitances and inductances for double steps, mitered bends with arbitrary angle, and asymmetric right-angle bends," *IEEE Trans. Microwave Theory Techn.*, vol. 28, no. 11, pp. 1213–1217, Nov. 1980.
- [43] Y. Geng, J. Wang, Y. Li, Z. Li, M. Chen, and Z. Zhang, "A Ka-band leaky-wave antenna array with stable gains based on HMSIW structure," *IEEE Antennas Wireless Propag. Lett.*, vol. 21, no. 8, pp. 1597–1601, Aug. 2022.
- [44] Y.-L. Lyu, F.-Y. Meng, G.-H. Yang, D. Erni, Q. Wu, and K. Wu, "Periodic SIW leaky-wave antenna with large circularly polarized beam scanning range," *IEEE Antennas Wireless Propag. Lett.*, vol. 16, pp. 2493–2496, Jul. 2017.
- [45] Y.-L. Lyu, F.-Y. Meng, G.-H. Yang, P.-Y. Wang, Q. Wu, and K. Wu, "Periodic leaky-wave antenna based on complementary pair of radiation elements," *IEEE Trans. Antennas Propag.*, vol. 66, no. 9, pp. 4503–4515, Sep. 2018.
- [46] Y. D. Dong and T. Itoh, "Composite right/left-handed substrate integrated waveguide and half-mode substrate integrated waveguide," in *2009 IEEE MTT-S Int. Microwave Sym. Digest*, Boston, MA, USA, Jun. 2009, pp. 49–52.